Quantifying bond rupture during indentation fracture of soft polymer networks using molecular mechanophores

J. N. M. Boots and D. W. te Brake
Physical Chemistry and Soft Matter, Wageningen University & Research, Stippeneng 4, 6708WE Wageningen, The Netherlands

Jess M. Clough
Adolphe Merkle Institute, Chemin des Verdiers 4, Fribourg 1700, Switzerland

J. Tauber, J. Ruiz-Franco, T. E. Kodger, and J. van der Gucht[*]
Physical Chemistry and Soft Matter, Wageningen University & Research, Stippeneng 4, 6708WE Wageningen, The Netherlands.

Understanding the resistance of soft materials to puncture bears relevance to many fields. However, the complex mechanics during deep indentation make it difficult to disentangle how the different dissipation processes contribute to the fracture energy and how this depends on the molecular structure of the material. To investigate this, we perform deep indentation experiments with a flat-ended cylindrical probe on polymer networks containing the covalently incorporated mechanoluminescent bond rupture sensor 1,2-dioxetane. By carrying out the experiments inside an integrating sphere, we are able to quantify the number of ruptured bonds during puncture nucleation and propagation. We find that puncture is associated with significant diffuse damage, both prior to nucleation of the main crack and during crack propagation. Moreover, in agreement with earlier results for uniaxial extension, we show that puncture of double networks leads to strongly enhanced rupture in the prestretched sacrificial network, while fracture of the matrix network is much more localized. Finally, we complement the experiments with MD simulations that allow us to link the rupture processes to the distribution of tension in the networks.

I. INTRODUCTION

Soft polymer materials are lightweight and deformable, making them suited candidates for several applications among which are seals [1], tyres [2], vibration dampers, soft robotics [3], haptics [4,5], and biomedical applications [6,7]. However, their lifetime in many of these applications is limited by the damage that occurs during deformation or loading. One deformation mode that is particularly prone to cause damage is the indentation with a sharp object, which leads to puncture of the material at high enough forces. Understanding the resistance of soft materials to puncture bears relevance to many fields, including punctures in tyres [8], forensic studies [9], bite mechanics [10], surgery [11], and design of protective clothing [12]. However, compared to the mechanics of fracture in other deformation modes, such as uniaxial extension and uniform compression, puncture mechanics is relatively poorly understood, mostly due to the heterogeneous, strongly localized, and nonlinear deformation field that arises during deep indentation and the role of friction and adhesion between the indenter and the material. Recently, Fakhouri, Hutchens, and Crosby studied the large strain behavior of soft elastomers during deep indentation, and they developed a model to predict how the critical indentation force at which

puncture starts depends on the size and shape of the indenter [13]. Experimental studies show that the shape of the crack that accompanies puncture is very sensitive to the geometry of the punch tip. While deep indentation with a sharp, conical punch leads to a planar mode-I crack [14], a flat-bottomed cylindrical punch penetrates a soft material by the formation of a ring-shaped mode-II crack that propagates ahead of the indenter tip [15]. A micromechanical model, developed by Shergold and Fleck [16], relates the penetration force to the strain energy stored in the material and the fracture energy needed to propagate the crack. However, it remains unclear how different dissipation processes contribute to the fracture energy and how this depends on the molecular structure of the material. Recent work on the uniaxial extension of elastomers shows that delocalized bond rupture in a large, diffuse zone around the crack tip can greatly enhance the fracture energy [17]. It is unclear, however, to what extent diffuse bond rupture also plays a role in the resistance to puncture and penetration. To make progress in our understanding, and to arrive at a microscopic picture of the puncture process, both for the crack nucleation and propagation stages, there is a clear need for methods that can quantify bond rupture during puncture.

In the past decade, knowledge about molecular scale fracture mechanics gained momentum through mechanochemical tools, such as molecular mechanophores that elicit an optical signal in response to mechanical activation [18,19]. A particularly powerful mechanophore for fracture studies is

---

[*]Author to whom correspondence should be addressed: jasper.vandergucht@wur.nl
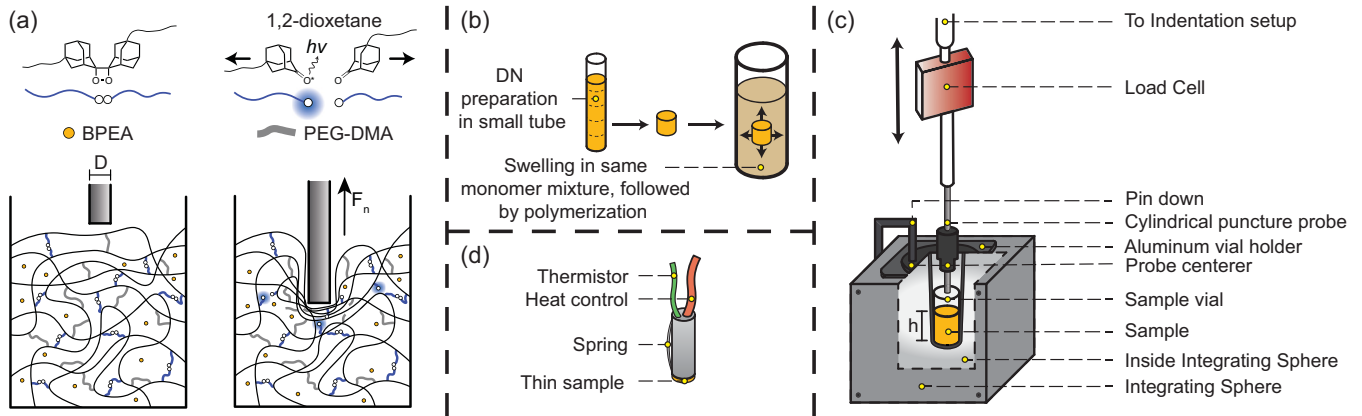
FIG. 1. (a) Mechanically induced chemiluminescence of a single dioxetane bond (top), BPEA fluorophore and PEG-DMA crosslinker (center), and schematic representation of the rupture of multiple dioxetane crosslinkers and some PEG-DMA crosslinkers in a strained polymer network during a deep indentation with a flat-bottomed cylindrical punch of diameter D (bottom). Photons emitted by bond scission events enable quantification of bond rupture during puncture. (b) Schematic of the synthesis scheme for the double network (DN): The first network is swollen in the same monomer mixture, which is then polymerized. (c) Schematic representation of the puncture experiment, conducted in an integrating sphere. The vial [28] containing the sample was held in place with an aluminum vial holder. After the sample vial was loaded, a 3D printed probe centerer was placed on top of the aluminum vial holder, ensuring puncture to occur in the lateral center of the sample. The puncture was done with custom-made cylindrical rods with flat bottoms of varying size, which were connected to a load cell to measure the force as a function of penetration depth. (d) Schematic of the heating element that was used for the heating experiments. Note the spring on the left of the element, which is a key factor that enables a secure position of the probe in the sample vial.

the mechanoluminescent probe bis(adamantyl)-1,2-dioxetane [20], which can be covalently incorporated in polymeric materials, for example, by introducing it as a crosslinker in polymer networks produced by free radical polymerization. The 1,2-dioxetane molecule releases energy in the form of light after being subjected to a thermal or mechanical stimulus that leads to bond rupture [see Fig. 1(a)]. Upon rupture, the carbon-oxygen ring in the dioxetane crosslinker breaks leading to two adamantones, of which one can be in the excited singlet or triplet state, which in turn can relax to the ground state by fluorescence [21,22], thereby emitting a photon. Previous work using this mechanophore sheds light on the shape, size, and location of the fracture process zone around a propagating crack tip in elastomers subjected to uniaxial tension [17]. These measurements also clearly illustrated the importance of the molecular architecture of the polymer networks, showing strongly enhanced bond rupture in so-called double networks consisting of two interpenetrating polymer networks, thereby providing experimental support for the molecular explanations put forward earlier for the enhanced toughness of such materials [23–27].

In this work, we use the same dioxetane mechanophores to detect bond rupture during deep indentation and puncture of soft crosslinked polymer materials, both single and double networks. To obtain a truly quantitative measurement of the number of broken bonds, we perform the experiment in an integrating sphere, so that all emitted photons can be detected. By simultaneously measuring the indentation force and the luminescent signal, we relate the mechanical response during different stages of penetration to the underlying molecular events. With the help of numerical mechanical simulations on model networks, this allows us to obtain a more detailed understanding of the microscopic processes occurring during indentation fracture.

II. MATERIALS & METHODS

A. Materials

We prepare networks made of poly(hexyl methacrylate), which is crosslinked using crosslinkers that can be mechanoluminescent (dioxetane-DMA) or optically inactive (PEG-DMA). Hexyl methacrylate (HMA) and polyethyleneglycoldimethacrylate (PEG-DMA, Mn=550 g/mol) were purified on an alumina column before use. Bismethacrylate functionalized bis(adamantyl)-1,2-dioxetane (dioxetane-DMA) was synthesized based on a previously published procedure [20], albeit with a different crosslinking functionality (see Supplemental Material (SM) [29]). 2,2'-azobis(2-methylpropionitrile) (AIBN), a thermal free radical initiator, and 9,10-bis(phenylethynyl)anthracene [30] (BPEA), a fluorophore that redshifts the dioxetane emitted photons [30]), were purchased from Sigma Aldrich and TCI chemicals and used without purification.

B. Synthesis of polymer networks

Single network (SN). Samples with different degree of crosslinking were synthesized, containing either a mixture of dioxetane-DMA to PEG-DMA in a ratio 1:3 as crosslinkers or with dioxetane-DMA as the only crosslinker, in this work indicated with a fraction $f = 0.25$ or $f = 1$ of the crosslinkers is a mechanoluminescent dioxetane molecule, respectively. For the synthesis of $f = 0.25$ networks, dioxetane-DMA (3.5 mg, 0.006 mmol) and AIBN (2.0 mg, 0.012 mmol) were mixed with 0.06 mL BPEA, stock solution of 2.5 g/L in toluene ($\lambda_{abs} = 455$ nm, $\lambda_{em} = 486$ nm) [31] and HMA (0.50 mL, 2.5 mmol) and PEG-DMA (0.0096 mL, 0.019 mmol) were added, resulting in a stoichiometry of HMA:PEG-DMA:dioxetane-DMA 99:0.75:0.25. Networks

with $f = 1$ were made in the same way, except that 14 mg (0.024 mmol) dioxetane-DMA was added and no PEG-DMA, resulting in a stoichiometry of HMA:dioxetane-DMA 99:1. These solutions were degassed with N_2 for 10 minutes. The mixture was allowed to polymerize in the oven at 70 °C for 2h. Before removing the cap, the solution was allowed to cool down and left at room temperature (RT) for two hours to continue the polymerization. Any remaining volatiles were removed at 70 °C under vacuum overnight, slightly shrinking the samples. To maximize contact of the sample with the bottom of the vial, samples were centrifuged at 5000 rpm for five minutes, resulting in samples with a height of ~15 mm with negligible shrinkage due to the centrifugation. Yet, a small void between the sample and the sides of the vial remained present for most samples.

All experiments reported here were performed with the same batch of dioxetane, ensuring that the luminescent properties were equal for all puncture tests.

Double network (DN). First, the first network of the double network is synthesized in an NMR tube with a diameter of 3.9 mm, following the protocol of the single network, see Fig. 1(b). The resulting network is cut in pieces with a height of 7 mm using a scalpel. Then, the network was swollen for two days in a monomer mixture containing HMA (0.30 mL, 1.52 mmol), PEG-DMA (0.007 mL, 0.015 mmol), AIBN (0.001 mg, 0.007 mmol), and 0.033 ml of a 2.5 g/L solution of BPEA in toluene, isotropically stretching the chains of the network. The obtained isotropic prestretching [32] was 1.65, see Fig. 5S in the SM. After degassing with N_2, the same protocol as for the SN was followed to polymerize the second network to obtain the DN.

C. Experimental methods

Indentation experiments. Indentation tests were performed using cylindrical punches (with a diameter of 1 or 0.7 mm) with a flat end. The indentation tests were performed with the sample placed in an integrating sphere (Thorlabs, IS200), see Fig. 1(c). The integrating sphere was connected to an APD detector (ALV-7004 Digital Correlator) with an optical fiber (Thorlabs, FP600URT). An in-house written script was used to record the collected photons at a frequency of 1250 Hz. Movement of the puncture probes and readout of the load cell were controlled using MATLAB [33]. All puncture tests were performed at RT. For the cyclic loading experiments, samples had to be immobilized to prevent movement of the sample during retraction due to adhesive and friction forces between the sample and the puncture probe. Therefore, the vial was fixed with the 3D printed probe centerer, which in turn was pinned down physically with two bars from the top, as shown in Fig. 1(c).

Calibration of the dioxetane emission. To convert the photon count measured in the integrating sphere into the number of broken dioxetane bonds, we performed a calibration experiment in which we heat a sample in the integrating sphere to 230 °C using the heating element [34] shown in Fig. 1(d), leading to thermally activated chemiluminescence [35]. We heated the sample for 3000 seconds, at which point the emission has returned to the noise level and all dioxetane bonds have decomposed thermally (see Fig. 8S in the SM). By

comparing the total thermoluminescent photon count in this heating experiment to the mechanoluminescent photon count in the puncture experiments (both corrected for background noise), we can estimate the number of broken bonds n_b corresponding to a certain photon count c_p:

$$n_b = \frac{\Phi_T}{\Phi_M} \frac{N_{b,T}}{N_{p,T}} c_p, \tag{1}$$

where $N_{b,T}$ is the total number of dioxetane bonds present in the thermally decomposed reference sample, which are all assumed to break, $N_{p,T}$ the total photon count in the reference experiment, and the ratio Φ_T / Φ_M corrects for the difference in chemiexcitation yield between thermally activated and mechanically activated dioxetane, with $\Phi_T \approx 17\%$ [35] and $\Phi_M \approx 9.8\%$ [36]. Note that n_b denotes the number of broken bonds during one acquisition interval of 0.8 ms. The cumulative number of broken bonds up to a certain strain $\Sigma n_b(\delta)$ can then be obtained by integration. We assume that the photon capture efficiency is not affected by the presence of the puncture probe or heating element, because both are made from materials that reflect most of the light. Furthermore, while the different sizes of the probe and the heating element might influence the leakage of photons from the integrating sphere slightly, the overall photon leakage is so small that these differences are expected to be negligible. More details about the calibration can be found in the SM.

D. Simulations

Single network (SN). We model the polymer network using a two-dimensional network model. We start by placing monomers on a triangular network of $N \times N$ nodes with $N = 170$ and lattice spacing l_0. Neighbouring monomers are then connected to each other with a probability $p_1 = 0.7$, and dangling bonds, which are elastically inactive, are removed from the network. Between each connected pair of nodes, a polymer chain of $N_m = 6$ connected monomers are inserted, resulting in an overall crosslink density of 8.7%. Here, crosslinkers are defined as nodes that connect at least three chains.

The excluded volume interaction is described by the Weeks-Chandler-Andersen (WCA) potential to mimic excluded volume, defined as [37]

$$V_{\text{WCA}}(r) = \begin{cases} 4\epsilon\left[\left(\frac{\sigma}{r}\right)^{12} - \left(\frac{\sigma}{r}\right)^{6}\right] + \epsilon & \text{if } r \leqslant 2^{1/6}\sigma \\ 0 & \text{otherwise} \end{cases}, \tag{2}$$

where σ is the diameter of a monomer, used as the unit length, and ϵ controls the energy scale. The networks were equilibrated in two steps, using *NPT*-ensemble simulations with a Nosé-Hoover thermostat [38]. In the first step, we equilibrate the network without allowing for bond rupture, by using a finite extensible nonlinear elastic (FENE) potential for the bonds between bonded neighboring monomers, expressed as [39]

$$V_{\text{FENE}}(r) = -\epsilon k_F R_0^2 \ln\left[1 - \left(\frac{r}{R_0 \sigma}\right)^2\right], \tag{3}$$

where $k_F = 15\epsilon/\sigma^2$ is the dimensionless spring constant and $R_0 = 1.5\sigma$ is the maximum extension of the bond. The mass of all particles is m, and hence, here and in the following, we express all quantities in reduced units: $[T] = \epsilon/k_B$ for the

TABLE I. Four different quartic potentials V_Q used with four different values of the parameter k_Q. The bond energy (the minimum of the potential) and the rupture force (calculated as the maximum value of dV_Q/dr) are also listed for each potential (in reduced units).

Bond type	k_Q	V_{min}	F_{max}
Strong	4751	−153	486
Weak-I	4251	−136	435
Weak-II	3651	−117	373
Weak-III	2351	−75	241

temperature, $[P] = \epsilon\sigma^{-2}$ for the pressure, and $[t] = \sqrt{m\sigma^2/\epsilon}$ for time, where k_B is the Boltzmann constant. In this mode, the energy minimum is found at $r_{min} = 0.96$. We fix $P = 0.0$ and $T = 1.0$, allowing anisotropic fluctuations of the periodic simulation box during 10^6 steps.

Next, we change the potential to a quartic potential, which allows us to model fracture processes in a realistic way [40,41]:

$$V_Q(r) = k_Q(r - R_c)^3(r - R_c - B_1), \quad (4)$$

where R_c is the cutoff radius that establishes the maximum bond length. Bonds break irreversibly if the bond length r exceeds R_c. We consider several different types of bonds in our simulations, with parameters as specified in Table I (plots of the different potentials can be found in Fig. S6b). In particular, the mechanoluminescent dioxetane crosslinkers used in the experiments are known to have a lower rupture force than the other covalent bonds in the polymer network. We therefore denote the bonds in the main chain of the polymers and of the nondioxetane crosslinkers as 'strong' bonds, while the dioxetane bonds are denoted as 'weak' bonds; three types of weak bonds, varying in rupture force as governed by the parameter k_Q, are considered (see Table I). The parameter B_1 is fixed at -0.7425 and $R_c = 1.5$ in all cases. The energy minimum is closer to $r_{min} = 0.96$, which is also the same as that for the FENE potential, so that any artificial stress accumulated after the change of the potential is minimized. However, before starting the indentation simulation, the network is re-equilibrated in the same way with the new potential. Note that bonds can in principle break during the second equilibration step, but we did not observe any bond rupture.

Double network (DN). Double networks (DN) are modelled by adding a second type of polymers between the crosslinkers defined previously in the single network. We choose a connectivity of $p_2 = 0.55$ for this second network (denoted DN-II), which ensures that the second network is fully percolated but has a lower crosslink density than the first network, as is also the case in experimental DNs [42]. In the experimental networks, the prestress in the first network (denoted DN-I) resulting from the swelling step causes bonds in the first network to be more prone to rupture than those in the second network. Here, we account for this by assigning a weaker potential ('weak-III,' see Table I) to the crosslinks in the first network and a 'strong' potential to the crosslinks in the second network. The networks are equilibrated again in two steps, similar to the SN.

Indentation simulations. The indentation of the networks is simulated in the *NVT* ensemble using Langevin dynamics.

Here, the friction coefficient of the monomers is fixed at $\xi_F = 1.0$. Periodic boundary conditions are considered in the horizontal direction (perpendicular to the direction of indentation), while reflective walls are used at the top and bottom edges. The indenter is modeled as a collection of $N_x \times N_y$ overlapping spherical particles of diameter $\sigma_I \geqslant 10\sigma$ (see Fig. S6c) that interact with the monomers by the WCA potential previously defined. This set of particles behaves as a rigid solid moving with a velocity $\mathbf{v}_I = -|v|\hat{e}_y$, where $|v| = 0.01$ and $\hat{e}_y$ is the unit vector in the y direction. The indentation force is measured by averaging the force exerted on the particles at the bottom of the indenter (which we denote as the sensor). We compare several indenter widths, $D = 22\sigma$, 32σ, 44σ, and 68σ.

Equilibration and puncture simulations are carried out using the LAMMPS simulation package [43] with a simulation time step $\Delta t = 0.002$. The results are averaged over two system realizations for each set of parameters. Additional information is shown in the SM.

III. RESULTS & DISCUSSION

A. Puncture of single networks

To allow for quantification of the number of broken bonds during puncture, we prepare HMA polymer networks in which a fraction $f = 0.25$ of the crosslinkers is a mechanoluminescent dioxetane molecule [Fig. 1(a)]. We then perform indentation experiments with a flat-bottomed cylindrical punch of diameter D inside an integrating sphere, while simultaneously measuring the force F_n as a function of indentation depth δ [Fig. 1(c)]. This setup does not allow us to obtain spatial information about the rupture of bonds; however, it does enable us to collect all photons emitted by ruptured dioxetane bonds, which is required for obtaining quantitative information about the number of broken bonds.

A typical force-distance curve is shown in Fig. 2(a) (top panel). The force curve is nonlinear, with a prepuncture response indicating a stiffness that increases with depth. Our data are in good agreement with previous work that reported a transition from a linear response $F_n \sim \delta$ at small depth to a quadratic response $F_n \sim \delta^2$ for deeper indentation (see Fig. 9S), which could be explained by modeling the material as a Neo-Hookean solid [13]. For small depth ($\delta < D$), the force response for a cylindrical punch in given by [44,45]:

$$F_n = DE^*\delta, \quad (5)$$

where $E^* = E/(1 - \nu^2)$ with E the Young's modulus of the material and ν the Poisson ratio, which is $\nu \approx 0.5$ for the nearly incompressible polymer networks that we use. From the initial slope of the force-depth curve we then find a Young's modulus on the order of 2 MPa for our samples [Fig. 3(a)].

At a critical depth δ_c, the indenter pierces through the surface of the material and the force drops abruptly. As the indenter continues to move down after a crack has nucleated, the force reaches a quasisteady state, which is significantly lower than the force at which the initial puncture takes place. In this stage of steady penetration, a ring-shaped crack propagates ahead of the indenter as it moves down [16]. Clearly, the
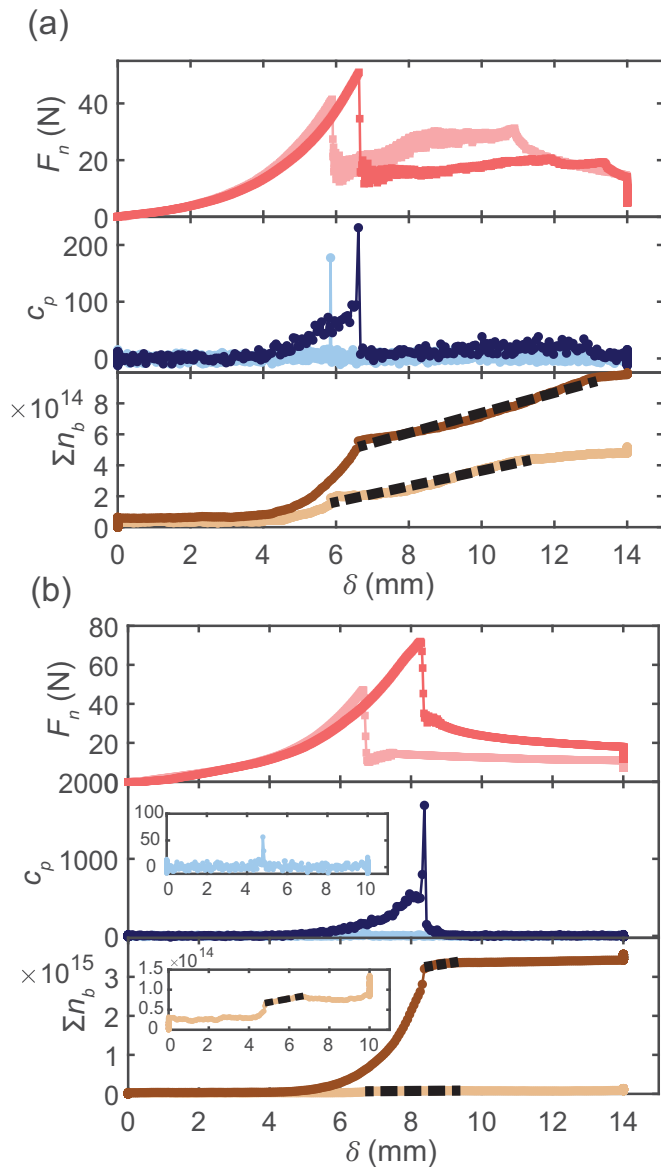
FIG. 2. The normal force F_n measured by the bulk load cell (top), the photon counts c_p recorded by the detector (middle), and the cumulative number of bonds broken Σn_b (bottom) as a function of the probe depth δ, for (a) a SN indented with a probe with $D = 1$ mm at $v = 2$ mm/s and, in lighter color in the background, $D = 1$ mm, and $v = 0.5$ mm/s, (b) DN-I with $D = 1$ mm at $v = 2$ mm/s and, in lighter color in the background, DN-II with $D = 1$ mm at $v = 2$ mm/s. Λ is deduced from the slope of the linear fits, indicated with dotted lines. Insets in the middle and bottom plots in panel (b) show the DN-II network at different y-axis scale. Please note the different scales on the vertical axes between panels (a) and (b).

force required to propagate the crack is smaller than the force required for nucleation.

The dioxetane emission c_p collected by the integrating sphere allows us to detect the rupture of bonds during the different stages of penetration. As shown in Fig. 2(a) (central panel), the dioxetane emission rises already before puncture occurs, and then shows a sharp peak during crack nucleation, indicating a large and abrupt rupture cascade accompanying

crack nucleation. After the crack has nucleated, the photon count reaches a steady but nonzero value, which reflects bond rupture as the crack propagates.

To convert the photon count into the number of broken bonds, we perform a calibration experiment using a reference sample in which dioxetane bonds are decomposed thermally inside the integrating sphere, as described in detail in the Methods section and the SM. The cumulative number of broken bonds Σn_b as the probe penetrates the sample as a function of depth is shown in Fig. 2(a), bottom panel. Again, we clearly see that bond rupture starts well before the main puncture event (which occurs at $\delta_c = 6.5$ mm for the experiment with a probe velocity of 2 mm/s and at $\delta_c = 5.8$ mm for a probe velocity of 0.5 mm/s). After the crack has nucleated, the cumulative bond rupture count increases linearly with δ, which agrees well with the idea of a crack that propagates steadily as the indenter moves down. From the slope of the curve, $\Lambda = \partial \Sigma n_b / \partial \delta$, we can estimate the width of the fracture zone. Assuming that the puncture occurs by forming a ring-shaped crack with a diameter that is comparable to the diameter D of the indenter [16], the surface area of the crack is $\pi D d$ with d the length of the crack, which is assumed to increase proportionally to δ. From this, we estimate the number of ruptured dioxetane bonds per unit crack area for this network as $\Sigma = \Lambda / \pi D = 1.4 \times 10^{19}$ m^{-2} for $v = 2$ mm/s, where the value of Λ is an average over 28 independently measured samples prepared in the same way. We can compare this number to the number that would be expected for a sharp crack surface as occurs for ideal brittle fracture, in which all bonds break in one single fracture plane; this can be estimated as $\Sigma_0 = f/(\xi^2)$ with ξ the average distance between crosslinks and where the factor f denotes the fraction of dioxetane crosslinkers relative to the total number of crosslinks, in this case equal to 0.25. We note that some of the crosslinkers may have reacted only at one end. In our estimate of Σ_0, we have implicitly assumed that the relative proportion of such inactive crosslinkers is the same for the dioxetane and PEG crosslinkers. Estimating ξ as $\xi \approx (E/3k_BT)^{-1/3}$, as expected from classical rubber theory, we find $\xi = 1.7$ nm, and $\Sigma_0 = 8.8 \times 10^{16}$ m^{-2}. Comparing Σ and Σ_0 we can define an enhancement factor α, which specifies the increase in bond rupture compared to the ideal brittle case

$$\alpha = \frac{\Sigma}{\Sigma_0} = \frac{\Lambda \xi^2}{f \pi D} \qquad (6)$$

For the present case, $\alpha \approx 160$, indicating that the fracture zone extends over a zone that is much wider than the mesh size, which also implies a large increase in the fracture energy. As is evident from post-mortem images of punctured samples, shown in Fig. 16S, this may be due to a wide and diffuse crack surface, to microcracks that radiate out from the main crack, or to irregularities in the crack shape.

We then repeated these measurements for a different probe diameter and indentation velocity (Fig. 3). For an indenter with a smaller diameter, $D = 0.7$ mm, we find that the critical penetration depth for rupture becomes roughly a factor of 1.75 lower, while the corresponding force decreases with a factor of 2.9 (Fig. 3a-2). This is in reasonable agreement with findings by Fakhouri, Hutchens, and Crosby [13], who found
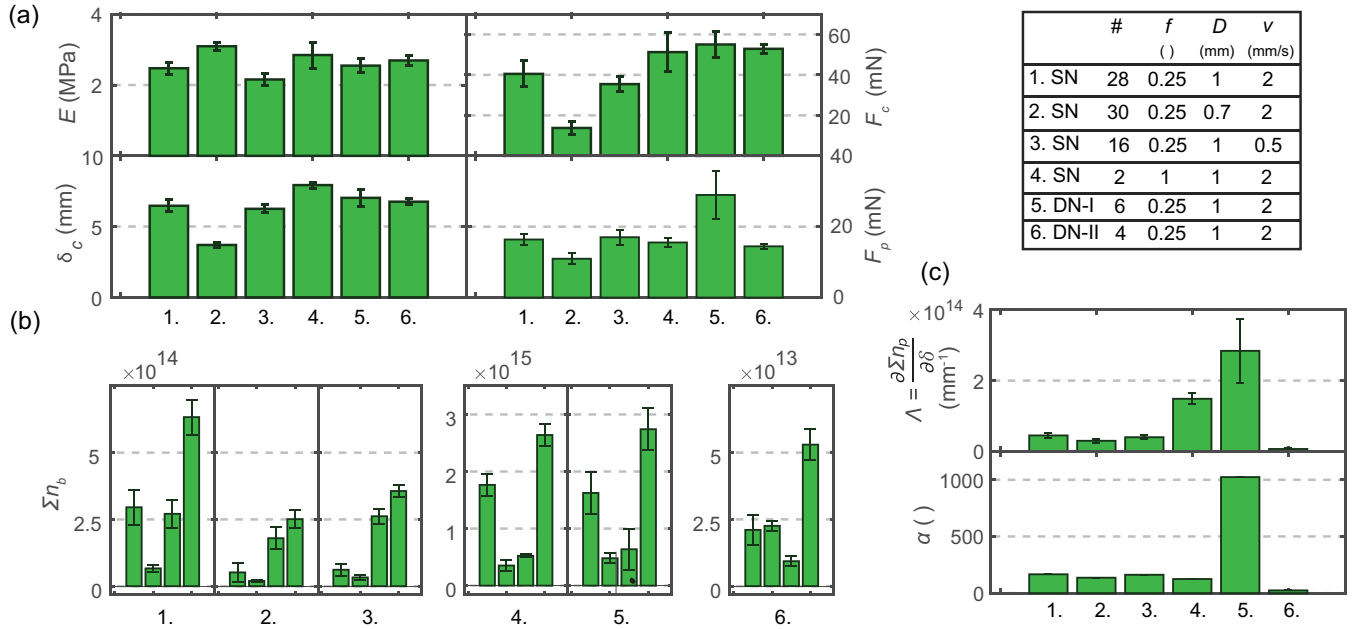
FIG. 3. (a) Bar plots of mechanical data; the elastic modulus E, the critical puncture depth at the main failure event δ_c, the critical normal force recorded by the bulk load cell at the puncture event F_c and the force during crack propagation F_p. (b) Bar plots showing the number of broken bonds before, during, and after the main failure event n_{prior}, n_{main}, n_{post} and their sum $\Sigma n_b = n_{prior} + n_{main} + n_{post}$, from left to right within each of the samples. Please note the varying scales on the y axes. (c) The number of broken bonds per unit crack length Λ and the enhancement factor α [Eq. (6)]. The numbers indicate different samples and conditions as specified in the table at the top right; (#) denotes the number of independent measurements for each configuration, (f) denotes the fraction of crosslinkers that is mechanoluminescent, (D) denotes the probe diameter, and v the probe velocity.

$\delta_c \sim D$ and $F_c \sim D^2$. The force F_p during the propagation stage is roughly 1.4 times smaller for the smaller probe, which corresponds to an increase in indentation pressure ($4F_p/\pi D^2$) by a factor 1.4 times, in qualitative agreement with earlier findings [16]. The number of bonds that break prior to and during the main puncture event are significantly smaller than for the larger probe (Fig. 3b-2), which indicates that crack nucleation is a much more localized event for this smaller probe size. For the propagation stage, we find that the number of bonds per unit crack length Λ decreases approximately proportionally to D, which means that the enhancement factor α, which characterizes the crack sharpness [Eq. (6)], is very similar to the one found for the larger probe (Fig. 3c-2).

Decreasing the velocity does not lead to a large change in the critical puncture depth and force (Fig. 3a-3). However, when looking at the broken bonds, we observe that the number of ruptured bonds prior to crack nucleation decreases by approximately a factor of 5 (Fig. 3 b-3). Apparently, the reduction in indentation velocity allows for additional stress relaxation mechanisms that reduce bond rupture. In the propagation stage, however, the effect of the velocity is much smaller, as can be seen from the enhancement factor α which decreases only by a factor 1.03 (Fig. 3c-3). Remarkably, the effect of probe velocity on bond rupture is much smaller during the crack propagation stage than during crack nucleation. Apparently, the dissipative processes around the crack front are less rate dependent in this velocity range than those involved prior to rupture; the origin of this difference is not clear.

The samples that we considered so far were crosslinked using a mixture of PEG-DMA and dioxetane DMA crosslinkers,

with $f = 0.25$. Since the dioxetane crosslinkers are weaker than other covalent bonds, the introduction of dioxetane linkers may affect the bond rupture process. To investigate this, we have also prepared samples with dioxetane crosslinkers only ($f = 1$). As shown in Fig. 3 a-4, the type of crosslinker does not have a significant effect on the Young's modulus, the critical puncture strain and force, and the force required for crack nucleation. As expected, the number of dioxetane bonds that break in these samples is higher than in the mixed sample for the same indenter diameter and indentation velocity (Figs. 3b-4 and 13S). In particular, the number of bonds that break before (n_{prior}) and during (n_{main}) the main puncture event is 5–6 times higher than for the mixed sample. Considering that the number of dioxetane bonds is four times higher in these samples, this suggests that the higher fraction of weak dioxetane bonds facilitates bond rupture. Such an enhancement is not observed during the propagation stage, as the enhancement factor α [Eq. (6)] is somewhat lower than for the sample with mixed crosslinkers (Fig. 3c-4), indicating a slightly sharper crack surface for the sample with only dioxetane crosslinkers.

B. Puncture of double networks

In the last decade, it has become clear that the resistance to fracture of a polymer material can be enhanced significantly by creating so-called double networks (DNs) [23]. In particular, tough DN elastomers have been made by swelling a first network in a liquid consisting of monomers that are then polymerized to form the second network [17,25]. The

first network (also called the sacrificial network), thus carries prestress due to the swelling and therefore tends to fracture before the second network (the matrix). This leads to large damage zones (microcracks) in the first network, which are held together by the intact matrix chains. Hence, the increased toughness is believed to result from the large number of sacrificial bonds that rupture upon fracture [17,25,41,42].

Here, we use our experimental set-up to study puncture of double network elastomers. We prepare DNs as described previously [17], while incorporating dioxetane crosslinkers (at $f = 0.25$) either in the first network (DN-I) or in the second (DN-II), see the Methods section. The force-depth curve for the DNs is very similar to that for the single networks, showing a significant increase in the stiffness with increasing strain, followed by an abrupt drop as the sample punctures [Fig. 2(b), top panel]. The critical depth and force and the elastic modulus are also comparable to those for the SNs (Figs. 3a-5,6), with the latter in line with a previous report [32]. The force for crack propagation is a bit higher in DN-I than for the single networks, which could be due to a higher toughness [14]; however, this is not the case for DN-II. Possibly, the crosslinking reaction in DN-II was less efficient than in DN-I, which could have caused this difference in propagation force. While the force response may not be very distinctive, the dioxetane emission is strongly increased for DNs with the dioxetane in the first network (see Figs. 2c and 3b-5), both before and after the main puncture event. This confirms the hypothesis for the toughening of DNs due to extra bond rupture in the sacrificial network. By contrast, for DN-II, which has the dioxetane in the second network, the emission is much lower than for the SNs (Fig. 3b-6), indicating very limited bond rupture in the matrix network. A similar behavior is seen in the propagation phase, where the parameters Λ and α are much higher than for the SNs if the dioxetane is in the first network, while they are much lower when the dioxetane is in the second network (Figs. 3c-5,6). Note, however, that for the DNs the propagation phase (as signified by the linear increase of Σn_b versus δ) extends only for a small range of depths; already long before δ reaches its maximum value, the bond rupture levels off and reaches a plateau, indicating that the crack propagation is halted. This is in contrast to the SNs, where bond rupture proceeds until the indenter is nearly at the bottom of the vial. This arrest of the crack propagation is confirmed by post-mortem images in Fig. 16S, which clearly show that the crack only proceeded through roughly half of the sample. This arrest of the crack is probably caused by the higher toughness of these materials, which prevents further crack propagation if not enough energy can be released.

Cyclic indentation of DNs. As shown above, most samples show significant bond rupture prior to the nucleation of a macroscopic crack. This accumulated damage should result in significant hysteresis and softening upon repeated loading, already before puncture occurs. We investigate this hysteresis for the DN-I sample, for which the photon emission is highest, by performing repeated indentation cycles at progressively increasing maximum depth δ_m, with five cycles for each depth [see Fig. 4(a)]. For this sample, macroscopic crack nucleation occurs in the first cycle of the series with $\delta_m = 14$ mm, as indicated by the large peak in the dioxetane emission. However, significant emission can be detected already in the earlier

cycles, indicating damage accumulation preceding fracture, similar to what we observed in the steady penetration data. As shown in Fig. 4(b), this accumulated damage leads to a softening of the material. In fact, this softening strongly resembles earlier observations on double networks under uniaxial tension, which were ascribed to the so-called Mullins effect [25]: in the later cycles, the indentation force is significantly lower on restraining below the maximum previously applied depth, see Fig. 10S. The area enclosed between the first loading to a certain depth and the reloading to that same depth is a measure for the irreversibly dissipated energy due to the accumulated damage. Note that this hysteresis energy is much smaller than the hysteresis between the approach and retract curves, which also includes viscoelastic dissipation and friction and adhesion between the probe and the material.

The corresponding dioxetane emission is shown in Fig. 4(c). Significant emission is detected only when δ_m exceeds 9 mm. The material does already soften at lower indentation depths, as shown in Fig. 4(b), but apparently this is not accompanied by significant emission. Possibly this is because the number of ruptured bonds in these cycles is too low to cause emission beyond the noise level. For deeper indentation, the dioxetane emission increased with increasing maximum depth. The emission in the first cycle at each δ_m is much higher than that in subsequent cycles, however. Moreover, significant light was emitted only when the depth reached a value that it had not yet reached before, indicating that few additional bonds were broken upon indenting again to the same depth. These data are in very good agreement with earlier observations of bond rupture during repeated tensile loading of filled elastomers [46].

To investigate the relation between the irreversible softening of the material and the number of broken bonds in more detail, we determine both the cumulative hysteresis energy E_h, determined by integrating the approach force over the indentation depth and taking the difference between subsequent cycles, and the cumulative number of broken dioxetane bonds Σn_b, both summed over all five cycles at a maximum depth δ_m (using the same calibration as used before). The two are plotted as a function of the depth δ_m in Fig. 4(d), while Fig. 4(e) shows the relation between the cumulative number of broken bonds and the total hysteresis energy. We find a linear relation between E_h and $\Delta \Sigma n_b$ in Fig. 4(e). We can obtain the energy dissipated per ruptured dioxetane bond from a linear fit to the data in Fig. 4(e), giving a value of approximately 2.8×10^4 kJ/mol. Comparing this to the energy required to mechanically rupture a dioxetane bond, which has been estimated to be around 50 kJ/mol [46], we see that roughly 0.2% of the dissipated energy is directly caused by rupture of the dioxetane bonds, similar to an earlier report for uniaxial loading of a filled elastomer [46]. The additional dissipation can be explained in part by the Lake Thomas theory for polymer fracture [47], which explains the enhanced fracture energy of polymers by the fact that stretching a polymer strand stores energy in all backbone bonds in the strand; rupture of one of the bonds then releases all this energy. Furthermore, the current methodology only reports rupture of dioxetane bonds, whereas other bonds, i.e. the PEG-DMA and the HMA backbone, also have to break around the tip, leading to an underestimation of the total number of ruptured bonds during
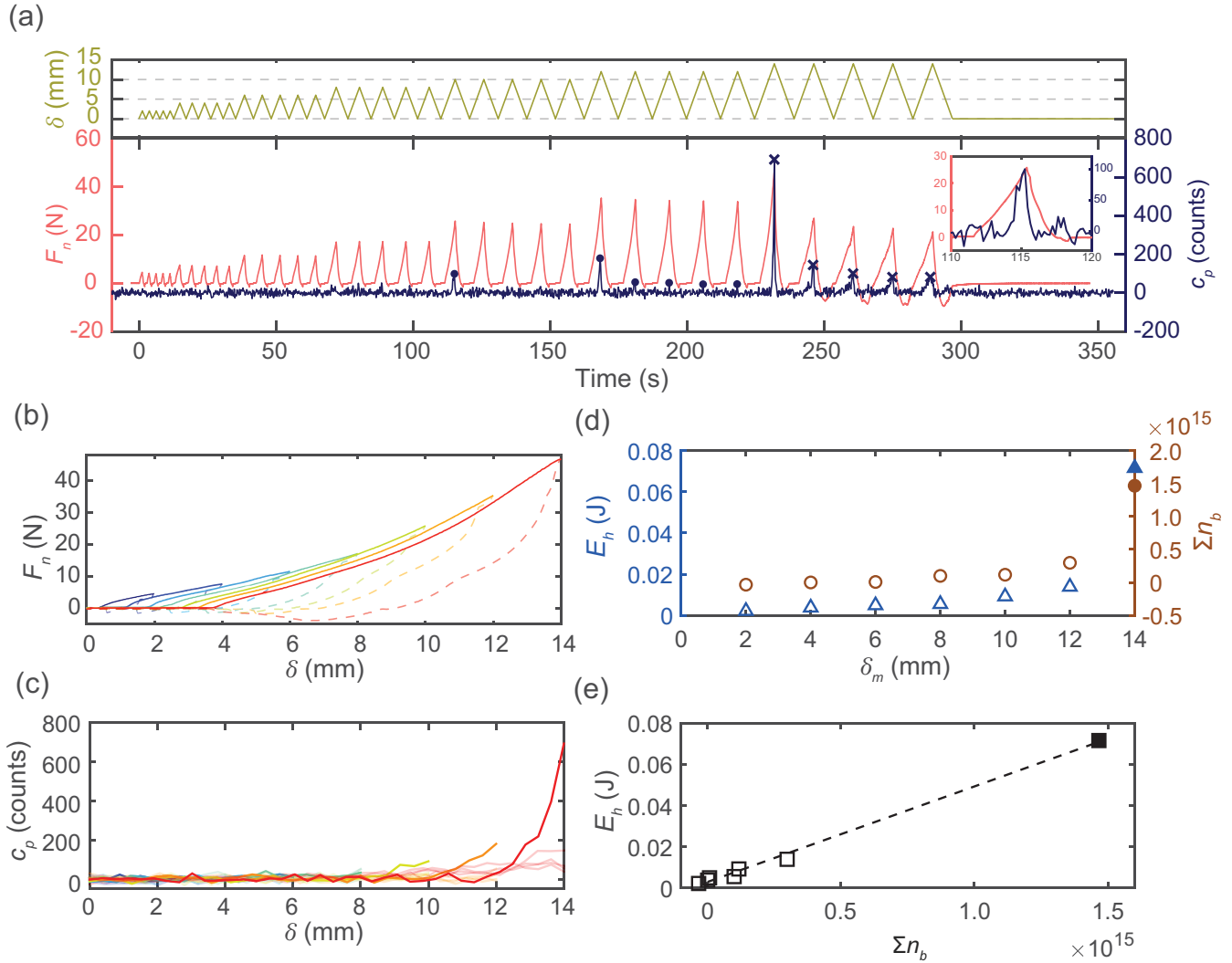
FIG. 4. (a) Cycling indentation tests of double network DN-I, showing the the depth δ (top) and the resulting force F_n in red and photon count c_p in blue (bottom) as a function of time. Circles and crosses indicate cycles where c_p exceeds the noise level before and after the main fracture event, respectively. The inset shows the first cycle with significant photon count. (b) Force-distance loops showing the first cycle of every depth; full curve is the approach and dashed curve the retract curve. (c) Photon counted by the detector c_p for all cycles with the first at each d_m plotted with zero transparency and the other four with some transparency. (d) The hysteresis energy E_h ($\triangle$) and the cumulative number of broken bonds Σn_b ($\circ$) both summed over 5 cycles at a maximum applied puncture depth δ_m, plotted versus δ_m. (e) E_h vs Σn_b both summed over five cycles at δ_m with the dashed line a linear fit, with the slope indicating the energy dissipated per broken dioxetane bond. Filled data points indicate data after the main fracture event.

the hysteresis tests. Lastly, it is very likely that additional dissipation mechanisms (such as friction or viscoelastic effects) contribute to the hysteresis energy [48]. We note that mechanical hysteresis is sensitive to the size of the sample; since in our experiments the sample thickness is not orders of magnitude larger than the indentation depth, the values we find are likely to be influenced by boundary effects.

C. Simulations

To obtain a more microscopic insight into the puncture process, we perform Molecular Dynamics (MD) simulations of the indentation process, using two-dimensional bead spring networks with quartic potential bonds (see Methods). During the simulations, we monitor the force exerted by the probe on

the network F, as well as the cumulative number of broken bonds Σn_b. We first consider networks in which all bonds have the same potential ('strong bonds,' see Table I), indented by probes of different diameter [Fig. 5(a)]. In agreement with the experimental observations, we find that F first rises nonlinearly due to elastic response of the material and then drops abruptly as the probe punctures the material. After the drop the force reaches a steady value around which it fluctuates as the probe moves further downward. Similarly to the experimental force curves [Fig. 3(a)], the critical depth δ_c and force F_c at rupture and the propagation force F_p increase as the probe diameter increases. The evolution of the number of broken bonds Σn_b [Fig. 5(a), lower panel] also follows a similar trend as observed experimentally [Fig. 2(a)]: Bond rupture starts already before the main puncture event, then increases
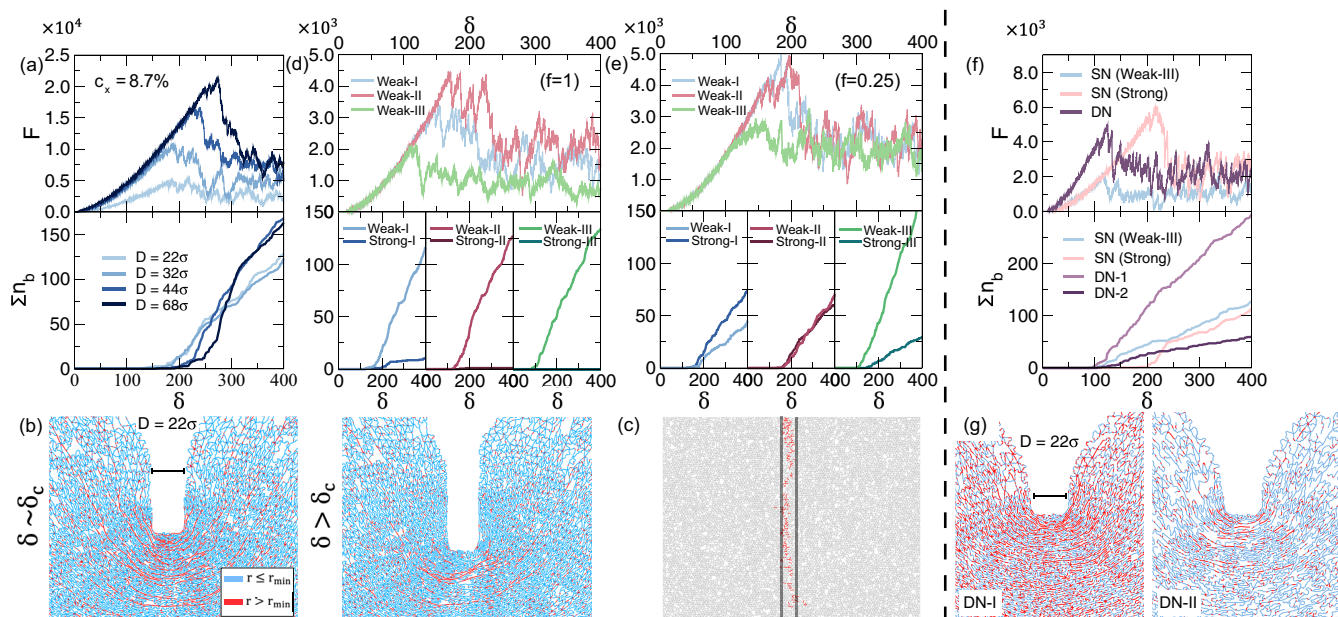
FIG. 5. (a) Force F and cumulative number of bonds broken Σn_b as a function of the probe depth δ for SN's with crosslinker concentration $c_x \sim 8.7\%$. (b) Snapshots of the SN with $c_x \sim 8.7\%$ and $D = 22\sigma$, at $\delta \sim \delta_c$ and $\delta < \delta_c$. (c) Broken bond position regarding the rest network. The vertical lines indicate the size D of the probe. (d) F and Σn_b as a function of δ for SN's with 100% of crosslinks with weak bonds, punctured with a probe size $D = 22\sigma$. (e) Same information for SN's with 25% of crosslinks with weak bonds. (f) F and Σn_b for a DN punctured with a probe of $D = 22\sigma$, having DN-I $c_x \sim 8.7\%$. Here, we compare the mechanical response of the DN with the single DN-I in the cases where the bonds are defined as strong (*SN-strong*) or weak (*SN-weak*). Likewise, Σn_b is split in broken bonds on DN-I and DN-II, respectively. (g) Snapshots showing the distribution of stretched bonds (red color) on the DN-I and DN-II.

significantly around the peak force (as seen by the increase in slope) before reaching a more or less constant slope within the crack propagation phase. Both the number of broken bonds before and during the main fracture event, and the slope Λ of the curves in the propagation phase, increase with increasing probe diameter (see Figs. 19S and 20S), in agreement with the experimental results shown in Figs. 3(b) and 3(c).

Figure 5(b) shows snapshots that highlight the distribution of tension in the polymer chains underneath the indenter for indentation depths around and after the peak force, with stretched bonds shown in red. Just before crack nucleation ($\delta \sim \delta_c$), the stretched bonds form long 'force chains' around the probe. Bond rupture then partially relaxes these force chains, and after crack nucleation the distribution of stretched bonds is more irregular, although the force chains can still be observed in the right panel in Fig. 5(b). We note also that the stretched bonds occur predominantly a small distance ahead of the indenter, so that the crack also propagates ahead of the probe. Remarkably, the rupture can be postponed by increasing D, which can be explained by the presence of stretched bonds occupying areas farther away from the front of the indenter, indicating thus a delocalization of stress (see Fig. 21S). Analyzing the distribution of broken bonds, we find that bond rupture occurs underneath the indenter, while the rest of the network remains undamaged [Fig. 5(c)]. Similar scenarios are found for different diameter probes and for different degrees of crosslinker, as shown in the SM Fig. 22S. We note, however, that the propagation of the crack is likely to occur in a different way than in the experiments, because the simulations are performed for two-dimensional networks, where a ring-shaped crack cannot develop. Moreover, while

the experimental probes are many orders of magnitude larger than the mesh size of the networks, in the simulations the difference is only one order of magnitude, so that the probe is comparatively sharper in the simulations.

Next, we consider networks consisting of mixtures of strong and weak bonds, to mimic the networks that contain dioxetane crosslinkers, which are known to be weaker than other covalent bonds. Since the relative rupture force of dioxetane bonds compared to other covalent bonds is not precisely known, we consider three different weak potentials, as specified in Table I. In the case where all crosslinkers are weak bonds while the backbone bonds are strong ($f = 1$), we find that the rupture force first increases as the strength of the weak bonds increases, although the weak-II case here shows a slightly higher peak force than the weak-I [Fig. 5(d)]. We believe, however, that the difference in peak force between weak I and weak II is within the simulation error, because the stochastic nature of crack nucleation leads to relatively large differences in the moment of fracture, especially for these relatively small systems. Likewise, the large majority of bonds that break are (weaker) crosslinks, although for the weak-I potential, whose rupture force $F_{max} = 435$, being the smallest difference with the strong bonds also some backbone bonds are ruptured. In the case where only 25% of the crosslinks are weak bonds ($f = 0.25$), we observe that the exact nature of the potential has less influence on the puncture process [Fig. 5(e)]. Thus, for the weakest crosslinks, weak III, characterized to have $F_{max} = 241$, rupture occurs predominantly at the weakest links, but upon reducing the difference in strength, we see more and more strong bonds that rupture (see also Fig. 19S). This shift illustrates the balance between

the localization of stresses in the network and the strength of the bonds in determining the pattern of bond rupture: In the presence of a significant amount of very weak bonds (weak III), fracture occurs predominantly by rupture of weak bonds, and hence the location of these weak bonds determines how cracks propagate. On the other hand, for the weak-I case, for which the difference in bond strength is smaller, the distribution of mechanical stress becomes more important, and thus strong and weak bonds have roughly the same probability to break. Comparing Figs. 5(d) and 5(e), we can see that for weak III, the number of broken weak bonds depends only weakly on their relative fraction in the network f, while for weak I, the number of broken weak bonds increases strongly as f goes from 0.25 to 1. The latter is closer to our experimental findings in Fig. 3(b), where the number of broken dioxetanes was found to increase more or less proportionally to f. This suggests that the difference in bond strength between the dioxetane bonds and the other bonds is relatively modest.

Finally, we perform simulations on the puncture of double networks. As explained in the methods section, we account for the prestretch in the first network DN-I (also called sacrificial network) by assigning a weaker potential (of type weak III) to the crosslinks in this network. As shown in Fig. 5(f), we find that puncture of the DN occurs at roughly the same indentation depth as for the single network obtained by only considering DN-I, while the propagation force after crack nucleation is similar to that found for the strong network DN-II. Similarly to the experimental DNs [Fig. 2(b)], we find a strongly enhanced number of broken bonds in the first network DN-I, while the number of broken bonds in the second network DN-II is reduced [Fig. 5(f), lower panel]. The number of ruptured bonds in DN-I is also higher than that in a single network with the same topology and bond potential, which indicates that the enhanced rupture is not due to presence of weaker bonds, but due to the interplay between the two networks. To further illustrate that, we present snapshots showing the distribution of tension in the two parts (at $\delta \sim \delta_c$) of the DN in Fig. 5(g). Clearly the stresses are much more delocalized in DN-I, with stretched chains occurring in a much larger region than for the single networks. This delocalization of stress is the origin of the enhanced bond rupture in DN-I, and hence, it translates in a higher width fracture zone on the DN-I (see Fig. 24S). We note, finally, that the reduction of the number of broken bonds in DN-II compared to DN-I is much less pronounced in the simulations [Fig. 5(f)] than in the experiments [Fig. 2(b)]. This difference could be due to the simplifying approximations in our model, such as our approach to account for prestretch in the first network by assuming a weaker potential, the limited system size, and the fact that our simulations are carried out in 2D instead of 3D. Alternatively, bond rupture in the experimental DN-II may be underestimated by incomplete polymerization and crosslinking in the second network due to the constraints imposed by the first network.

IV. CONCLUDING REMARKS

In this work, we have used mechanoluminescent molecular probes to obtain a detailed and quantitative insight in the bond rupture processes that occur during puncture of polymer materials. We have demonstrated that significant bond rupture occurs already before the probe penetrates the surface of the material and a drop in indentation force can be seen. Once the probe has pierced through the surface, further penetration proceeds by the propagation of a ring-shaped crack. By quantifying the number of broken bonds in this stage, it is clear that this crack is associated with a damage zone of significant size. Furthermore, we have shown that the puncture of double network involves a strongly enhanced rupture of bonds in the first, sacrificial network. By comparing to computer simulations of model networks, we find that this is due to a delocalization of the stresses in a large zone around the indenter.

We anticipate that the methods presented here can be used to address multiple interesting scientific questions such as the effects of indenter geometry, network topology, crosslink density, plasticizers, and viscoelastic stress relaxation on puncture mechanics. Finally, while the use of the integrating sphere prevents us from obtaining spatial information, it may be possible to map out the spatial distribution of bond rupture events during puncture by using a high-sensitivity camera.

[1] K. Sotoodeh, A review of valve stem sealing to prevent leakage from the valve and its effect on valve operation, J. Failure Analys. Prevention **21**, 9 (2021).

[2] F. Alkadi, J. Lee, J.-S. Yeo, S.-H. Hwang, and J.-W. Choi, 3d printing of ground tire rubber composites, Inte. J. Precision Eng. Manufacturing-Green Technology **6**, 211 (2019).

[3] C. Majidi, Soft-matter engineering for soft robotics, Adv. Mater. Technologies **4**, 1800477 (2019).

[4] H. A. Sonar, A. P. Gerratt, S. P. Lacour, and J. Paik, Closed-loop haptic feedback control using a self-sensing soft pneumatic actuator skin, Soft Robotics **7**, 22 (2020).

[5] S. Li, H. Bai, R. F. Shepherd, and H. Zhao, Bio-inspired design and additive manufacturing of soft materials, machines, robots, and haptic interfaces, Angew. Chem., Int. Ed. **58**, 11182 (2019).

[6] H.-J. Jeong, H. Nam, J. Jang, and S.-J. Lee, 3d bioprinting strategies for the regeneration of functional tubular tissues and organs, Bioengineering **7**, 32 (2020).

[7] S. Cascone and G. Lamberti, Hydrogel-based commercial products for biomedical applications: A review, Inte. J. Pharmaceutics **573**, 118803 (2020).

[8] F. Cecchini, V. Cherubini, M. Sadaf, F. Fabbrocino, and F. Nanni, Design of a puncture-resistant composite shell comprising a non-newtonian core, Polymer Testing **67**, 494 (2018).

[9] B. Wong, J. A. Kieser, I. Ichim, M. Swain, V. Livingstone, N. Waddell, and M. Taylor, Experimental simulation of non-ballistic wounding by sharp and blunt punches, Forensic science, medicine, and pathology **4**, 212 (2008).

[10] S. Das, S. Laha, and A. Ghatak, A co-operative effect of closely spaced intruding objects puncturing into a soft solid, Soft matter **10**, 6059 (2014).

[11] A. M. Okamura, C. Simone, and M. D. O'leary, Force modeling for needle insertion into soft tissue, IEEE Trans. Biomed. Eng. **51**, 1707 (2004).

[12] R. Fangueiro, R. Carvalho, D. Silveira, N. Ferreira, C. Ferreira, F. Monteiro, and S. Sampaio, Development of high-performance single layer weft knitted structures for cut and puncture protection, J. Textile Sci. Eng. **5**, 2 (2015).

[13] S. Fakhouri, S. B. Hutchens, and A. J. Crosby, Puncture mechanics of soft solids, Soft Matter **11**, 4723 (2015).

[14] O. A. Shergold and N. A. Fleck, Experimental investigation into the deep penetration of soft solids by sharp and blunt punches, with application to the piercing of skin, Trans. ASME **127**, 838 (2005).

[15] A. Stevenson and K. Ab Malek, On the puncture mechanics of rubber, Rubber Chem. Technology **67**, 743 (1994).

[16] O. A. Shergold and N. A. Fleck, Mechanisms of deep penetration of soft solids, with application to the injection and wounding of skin, Proc. R. Soc. London Ser., A **460**, 3037 (2004).

[17] E. Ducrot, Y. Chen, M. Bulters, R. P. Sijbesma, and C. Creton, Toughening elastomers with sacrificial bonds and watching them break, Science **344**, 186 (2014).

[18] J. Slootman, V. Waltz, C. J. Yeh, C. Baumann, R. Göst, J. Comtet, and C. Creton, Quantifying and mapping covalent bond scission during elastomer fracture, arXiv:2006.09468.

[19] G. E. Sanoja, X. P. Morelle, J. Comtet, C. J. Yeh, M. Ciccotti, and C. Creton, Why is mechanical fatigue different from toughness in elastomers? the role of damage by polymer chain scission, Sci. Adv. **7**, eabg9410 (2021).

[20] Y. Chen, A. Spiering, S. Karthikeyan, G. W. Peters, E. Meijer, and R. P. Sijbesma, Mechanically induced chemiluminescence from polymers incorporating a 1, 2-dioxetane unit in the main chain, Nat. Chem. **4**, 559 (2012).

[21] J. C. Hummelen, T. M. Luider, and H. Wynberg, Functionalized adamantylideneadamantane 1, 2-dioxetanes: investigations on stable and inherently chemiluminescent compounds as a tool for clinical analysis, Pure Appl. Chem. **59**, 639 (1987).

[22] J. Hummelen, T. M. Luider, and H. Wynberg, *Thermochemiluminescence Immunoassay* (University of Groningen, Stratingh Institute for Chemistry, Groningen, 1988).

[23] J. P. Gong, Y. Katsuyama, T. Kurokawa, and Y. Osada, Double-network hydrogels with extremely high mechanical strength, Adv. Mater. **15**, 1155 (2003).

[24] Y. Tanaka, R. Kuwabara, Y.-H. Na, T. Kurokawa, J. P. Gong, and Y. Osada, Determination of fracture energy of high strength double network hydrogels, J. Phys. Chem. B **109**, 11559 (2005).

[25] R. E. Webber, C. Creton, H. R. Brown, and J. P. Gong, Large strain hysteresis and mullins effect of tough double-network hydrogels, Macromolecules **40**, 2919 (2007).

[26] H. R. Brown, A model of the fracture of double network gels, Macromolecules **40**, 3815 (2007).

[27] Y. Tanaka, A local damage model for anomalous high toughness of double-network gels, Europhys. Lett. **78**, 56005 (2007).

[28] VWR, Vwr international b.v., amsterdam, product number 1-NWV-C.

[29] See Supplemental Material at http://link.aps.org/supplemental/10.1103/PhysRevMaterials.6.025605 for details.

[30] M. Mitsui, Y. Kawano, R. Takahashi, and H. Fukui, Photophysics and photostability of 9, 10-bis (phenylethynyl) anthracene revealed by single-molecule spectroscopy, RSC advances **2**, 9921 (2012).

[31] D. Maulding and B. G. Roberts, Electronic absorption and fluorescence of phenylethynyl-substituted acenes, J. Organic Chem. **34**, 1734 (1969).

[32] P. Millereau, E. Ducrot, J. M. Clough, M. E. Wiseman, H. R. Brown, R. P. Sijbesma, and C. Creton, Mechanics of elastomeric molecular composites, Proc. Natl. Acad. Sci. **115**, 9110 (2018).

[33] *MATLAB version R2018b*, The Mathworks, Inc., Natick, Massachusetts (2018).

[34] *PCE-IR 51*, PCE Instruments, PCE Brookhuis B.V., Enschede, The Netherlands.

[35] G. B. Schuster, N. J. Turro, H. C. Steinmetzer, A. P. Schaap, G. Faler, W. Adam, and J. Liu, Adamantylideneadamantane-1, 2-dioxetane. chemiluminescence and decomposition kinetics of an unusually stable 1, 2-dioxetane, J. Am. Chem. Soc. **97**, 7110 (1975).

[36] J. M. Clough and R. P. Sijbesma, Dioxetane scission products unchanged by mechanical force, Chem. Phys. Chem. **15**, 3565 (2014).

[37] J. D. Weeks, D. Chandler, and H. C. Andersen, Role of repulsive forces in determining the equilibrium structure of simple liquids, J. Chem. Phys. **54**, 5237 (1971).

[38] G. J. Martyna, M. L. Klein, and M. Tuckerman, Nosé–hoover chains: The canonical ensemble via continuous dynamics, J. Chem. Phys. **97**, 2635 (1992).

[39] K. Kremer and G. S. Grest, Dynamics of entangled linear polymer melts: A molecular-dynamics simulation, J. Chem. Phys. **92**, 5057 (1990).

[40] T. Ge, F. Pierce, D. Perahia, G. S. Grest, and M. O. Robbins, Molecular Dynamics Simulations of Polymer Welding: Strength from Interfacial Entanglements, Phys. Rev. Lett. **110**, 098301 (2013).

[41] J. Tauber, L. Rovigatti, S. Dussi, and J. Van Der Gucht, Sharing the load: Stress redistribution governs fracture of polymer double networks, Macromolecules **54**, 8563 (2021).

[42] J. P. Gong, Why are double network hydrogels so tough?, Soft Matter **6**, 2583 (2010).

[43] S. Plimpton, Fast parallel algorithms for short-range molecular dynamics, J. Comput. Phys. **117**, 1 (1995).

[44] A. C. Fischer-Cripps, *Introduction to Contact Mechanics*, Vol. 101 (Springer, New South Wales, Australia, 2007).

[45] K. L. Johnson, *Contact Mechanics* (Cambridge University Press, Cambridge, UK, 1987).

[46] J. M. Clough, C. Creton, S. L. Craig, and R. P. Sijbesma, Covalent bond scission in the mullins effect of a filled elastomer: Real-time visualization with mechanoluminescence, Adv. Funct. Mater. **26**, 9063 (2016).

[47] G. Lake and A. Thomas, The strength of highly elastic materials, Proc. R. Soc. London A **300**, 108 (1967).

[48] T. T. Duncan, J. M. Sarapas, A. P. Defante, K. L. Beers, and E. P. Chan, Cutting to measure the elasticity and fracture of soft gels, Soft Matter **16**, 8826 (2020).